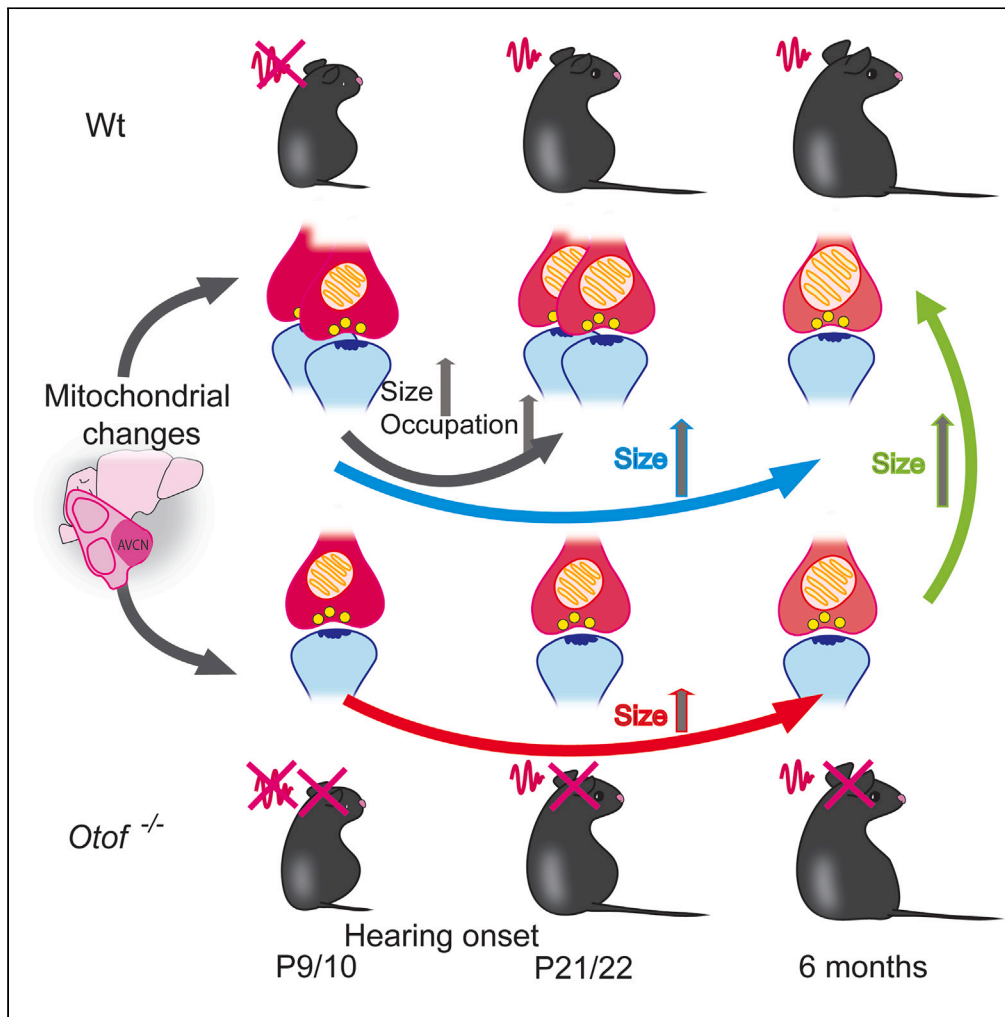# iScience

Article

Developmental changes of the mitochondria in the murine anteroventral cochlear nucleus

Anika Hintze, Felix Lange, Anna M. Steyer, Jannis Anstatt, Wiebke Möbius, Stefan Jakobs, Carolin Wichmann

sjakobs@gwdg.de (S.J.)
carolin.wichmann@med.
uni-goettingen.de (C.W.)

Highlights

Mitochondrial occupation in bouton-like synapses increases upon hearing onset

Mitochondria and crista membranes increase after hearing onset in wt endbulb synapses

Mitochondria and cristae membrane sizes slightly increase in endbulbs of deaf animals

Neuronal activity influences the size and inner architecture of AVCN mitochondria

Article

Developmental changes of the mitochondria in the murine anteroventral cochlear nucleus

Anika Hintze,[1,7] Felix Lange,[2,3,7] Anna M. Steyer,[4,5,8] Jannis Anstatt,[2,3] Wiebke Möbius,[4,5] Stefan Jakobs,[2,3,4,6,*] and Carolin Wichmann[1,4,9,*]

SUMMARY

Mitochondria are key organelles to provide ATP for synaptic transmission. This study aims to unravel the structural adaptation of mitochondria to an increase in presynaptic energy demand and upon the functional impairment of the auditory system. We use the anteroventral cochlear nucleus (AVCN) of wild-type and congenital deaf mice before and after hearing onset as a model system for presynaptic states of lower and higher energy demands. We combine focused ion beam scanning electron microscopy and electron tomography to investigate mitochondrial morphology. We found a larger volume of synaptic boutons and mitochondria after hearing onset with a higher crista membrane density. In deaf animals lacking otoferlin, we observed a shallow increase of mitochondrial volumes toward adulthood in endbulbs, while in wild-type animals mitochondria further enlarged. We propose that in the AVCN, presynaptic mitochondria undergo major structural changes likely to serve higher energy demands upon the onset of hearing and further maturation.

INTRODUCTION

Synaptic transmission poses a major energy consuming process in the brain, but how neurons maintain a constant energy supply during extended synaptic activity and how presynaptic mitochondria might change their morphology upon activity remains largely elusive. Mitochondria serve as the primary energy generators.[1] Moreover, they regulate neurotransmission by Ca^{2+} buffering[2–6] and contribute to other cellular processes such as signaling, the regulation of cell proliferation, cell migration, cell viability, and neuronal morphology.[7,8] Mitochondria exhibit as smooth outer membrane (MOM) and a highly folded inner membrane (IM). The IM can be structurally and functionally subdivided into the inner boundary membrane (IBM) that parallels the MOM and the crista membranes (CMs). The latter form invaginations into the mitochondrial matrix.[9,10] The CMs are strongly enriched for subunits of the respiratory chain. Structural changes in (i) the mitochondrial volume and/or (ii) the shape, volume and surface area of the CMs might reflect different energy demands of synapses. Mitochondrial networks at synapses are highly dynamic and can change depending on local needs. This includes changes in shape and size by fission and fusion as well as anchoring to specific positions or movements of mitochondria.[11]

Several studies indicated a coupling of the mitochondrial volume and ultrastructure to different levels of synaptic performance.[12–15] In hippocampal synaptosomes, the presence of larger presynaptic mitochondria is associated with higher levels of synaptic vesicle (SV) release.[13] Comparing high- and low-performing neurons of glutamatergic as well as GABAergic boutons within the hippocampal formation revealed larger mitochondria with a higher CM density at axonal release sites of high-performance neurons.[12] However, very little is known on the structural adaptation of mitochondria to different requirements in the auditory system.

The maturation of the auditory system is associated with an increase in neuronal activity. A high precision of synaptic transmission at auditory synapses is required due to sound localization and sound perception cues.[16] The first three synapses of the auditory pathway, the inner hair cell (IHC) ribbon synapse in the periphery, the endbulb of Held and the calyx of Held synapses, fulfill these requirements. A very important step in the maturation process is the hearing onset, which occurs in mice around postnatal day (P)11/12.[17] Before that, non-sensory

[1]Molecular Architecture of Synapses Group, Institute for Auditory Neuroscience, InnerEarLab and Center for Biostructural Imaging of Neurodegeneration, University Medical Center Göttingen, 37075 Göttingen, Germany
[2]Department of NanoBiophotonics, Max Planck Institute for Multidisciplinary Sciences, 37077 Göttingen, Germany
[3]Clinic of Neurology, University Medical Center Göttingen, 37075 Göttingen, Germany
[4]Multiscale Bioimaging Cluster of Excellence (MBExC), University of Göttingen, 37075 Göttingen, Germany
[5]Electron Microscopy-City Campus, Department of Neurogenetics, Max Planck Institute for Multidisciplinary Sciences, 37075 Göttingen, Germany
[6]Translational Neuroinflammation and Automated Microscopy, Fraunhofer Institute for Translational Medicine and Pharmacology ITMP, Göttingen, Germany
[7]These authors contributed equally
[8]Present address: Imaging Center, European Molecular Biology Laboratory Heidelberg, Germany
[9]Lead contact
*Correspondence: sjakobs@gwdg.de (S.J.), carolin.wichmann@med.uni-goettingen.de (C.W.)
https://doi.org/10.1016/j.isci.2023.108700

spontaneous activity already shapes the pathway.[18–20] Hearing is depending on the protein otoferlin, which is encoded by the *OTOF* gene and consists of six C_2 domains and a C-terminal transmembrane domain.[21] Mutations in the *OTOF* gene are associated with the genetic auditory synaptopathy called autosomal recessive non-syndromic deafness DFNB9,[22–24] due to its lack in the cochlear IHCs. More than 200 pathogenic *OTOF* mutations have been identified whereby most of them lead to profound deafness[25] due to a lack of Ca^{2+} dependent exocytosis at IHC ribbon synapses, which is almost completely abolished in otoferlin lacking mice. Consequently, otoferlin knock out ($Otof^{-/-}$) mice show no detectable auditory brain stem responses (ABRs).[26] Therefore, otoferlin mutant mice serve as a common model of congenitally deafness.

Endbulbs of Held harbor hundreds of individual active zones (AZs)[27–29] and are formed by auditory nerve fibers that relay auditory information to bushy cells (BCs) within the AVCN.[30] Though otoferlin is not a molecular component of brain stem synapses, mice that lack otoferlin show a reduced number of SVs at endbulb AZs upon adulthood[31] and endbulb terminals are fewer and smaller.[32] Spherical bushy cells (SBCs) further receive excitatory input by small regular bouton-like synapses from the auditory nerve at their dendrites. It has been suggested that these small contacts modulate auditory processing by improving the temporal precision and fidelity.[33] Other cell types can be found in the VNC such as the T-stellate cells that project out of the CN to numerous targets in the brainstem but also form contacts within the CN. T-stellate cells exhibit several different functions and thus encode a wide spectrum of sound.[34] Recently, Lin and co-workers found that T-stellate cells directly synapse on both the soma and dendrites of other T-stellate cells.[35] Consequently, auditory input might have a strong influence on synaptic morphometric parameters of different synapse types within the AVCN.

In this study, we determine changes in mitochondria morphology upon hearing onset and maturation toward adulthood in the AVCN. We ask, if hearing onset has a consequence on the mitochondria abundance or morphology and how the lack of auditory input affects mitochondrial volume and CM arrangement. We combined different electron microscopic techniques in order to quantify the abundance and morphology of mitochondria. We found that more presynaptic bouton-like terminals harbor mitochondria after hearing onset. Moreover, we observed larger mitochondria in endbulbs of Held of mature wild-type (wt) AVCNs but almost unchanged sizes in adult otoferlin mutants. Our results point toward a higher energy demand upon auditory input in synapses of the AVCN, which is satisfied by increasing mitochondrial volumes and CMs areas.

RESULTS

Mitochondria are increasing in volume in different synapse types in the anteroventral cochlear nucleus

In order to understand if the maturation process as well as changes in activity, namely the hearing onset, affects mitochondrial structure and distribution within the AVCN, we analyzed presynaptic mitochondria of different synapse types including bouton-like non-endbulb synaptic terminals and endbulb of Held synapses. The latter are clearly distinguishable by their specific morphology, as done in previous studies.[31,36] We used electron tomography in combination with high-pressure freezing/freeze substitution (HPF/FS) in order to resolve mitochondria and their membranous structures in both synapse types in a near-to-native state and with highest resolution. Figure S1 shows a typical endbulb of a P10 wt mouse making contact to a BC. Vesicle clusters that can be identified in the semithin-section and together with the size of the terminal these are clear criteria to identify endbulbs of Held. Please note that the typical curved structure from endbulb of Held AZs cannot be found in HPF/FS sample preparations,[31,37] likely due to the lack of initial chemical fixation and the gentle FS process to substitute cell water with acetone. Bouton-like, excitatory non-endbulb synapses were selected when projecting on dendrite-like structures and showing clear synaptic vesicle (SV) cluster. We determined a number of structural parameters, such as the mitochondrial volume, the CM surface area, the crista density and the shape factor of the CMs as well as the distance of the mitochondria to the nearest AZ. In order to understand how auditory input influences mitochondrial morphology, we compared P10 for the pre-hearing stage to P21 (young) wt mice.

Mitochondrial volumes increase at non-endbulb synapses from pre-hearing to young hearing mice

In a first step, we performed electron tomography of small excitatory, non-endbulb (abbreviated as synapses: syn) terminals as shown in Figures 1A and 1B. To this end, tomograms of bouton-like terminals were acquired and excitatory AZs were identified based on the presence of a clear postsynaptic density (PSD) as described in Hintze et al.[31] These synapses likely represent to a high proportion synaptic contacts on dendrites of BCs.[36] Notably, tomograms typically included only small parts of mitochondria due to the limitation of the section thickness to 250 nm. Therefore, changes in volume might partially be a result of different cutting planes throughout the mitochondria. To avoid a bias, we randomly picked mitochondria from different angles for each genotype and condition. These mitochondria were used for the manual segmentation of the MOM that allowed us to determine the mitochondrial volume (Figures 1A and 1B). We found an average mitochondrial volume of $0.008 \pm 0.005\ \mu m^3$ (all values in the text represent mean $\pm$ SEM and can additionally be found in Tables S1–S3) within these synaptic terminals of pre-hearing mice. Significantly larger volumes were found after the onset of hearing comparing all reconstructed mitochondria ($0.010 \pm 0.005\ \mu m^3$; p = 0.0167; Figure 1C). Since PSDs appear as fine filamentous structures in electron tomograms of high-pressure frozen tissue, we determined the part of the presynaptic membrane that was opposed to the PSD as the presynaptic AZ membrane, as done previously.[31] The average reconstructed AZ area was comparable with $0.047 \pm 0.017\ \mu m^2$ at P10 and $0.055 \pm 0.017\ \mu m^2$ at P21 (Figure 1D). Moreover, electron tomography revealed that mitochondria were highly variable in their size and shape, as exemplified on endbulb terminals Figure S2.

Mitochondria are sometimes found to be arranged in mitochondrion-associated adherens complexes (MACs) and anchored to the plasma membrane on average in 200 nm distance from AZs.[38] This complex formation was initially described in the spinal cord,[39] but also found in chemically fixed calyx and endbulb terminals.[27,36,38,40] In our high-pressure frozen samples, MACs could not be identified. However, a close distance of mitochondria to AZs could indicate their presence. Therefore, we determined the mean shortest distance of the reconstructed
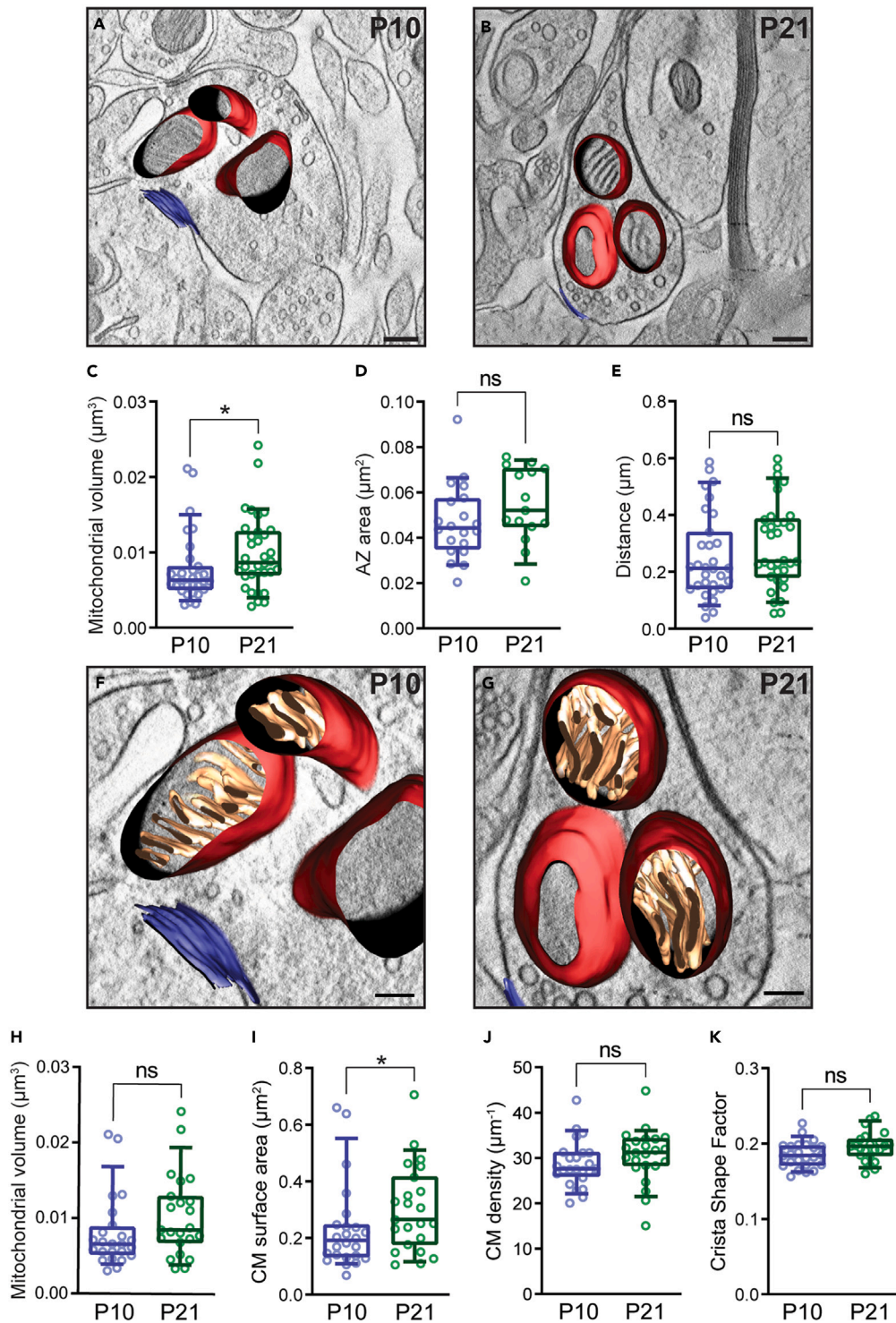
Figure 1. The ultrastructure of mitochondria at non-endbulb synapses is only slightly affected by the maturation of the auditory system

(A and B) 3D model showing the z-view of a tomogram to reveal AZ membranes (blue) and presynaptic mitochondria (red) within a non-endbulb terminal of P10 (A) and P21 (B) wt mice. Scale bars 200 nm.

(C) The volumes of all analyzed mitochondria are larger at P21 (p = 0.0167).

(D) The reconstructed AZ areas are similar between the age groups.

(E) The shortest distance of the mitochondria to the AZ membrane is comparable between P10 and P21.

Figure 1. Continued

(F and G) Higher magnifications of (A) and (B) showing examples of mitochondria in which the cristae could be reconstructed. Scale bars 100 nm.

(H) The volumes of this subset of mitochondria are not significantly different between both groups.

(I) The sum of surface areas of the CMs is larger after the onset of hearing (p = 0.0424).

(J) The CM density (CM surface area/mitochondrial volume) is comparable between P10 and P21.

(K) The lamellarity of the cristae is similar as verified by the crista shape factor (CM surface area/CM lumen volume). Box and whisker plots present median, lower/upper quartiles: 10-90th percentiles. ns, not significant; *p < 0.05; P10 (N = 3; n = 31/24) in blue and P21 (N = 3; n = 34/23) in green. (N: number of animals; n: number of mitochondria (all/with the segmentation of cristae). For details about values and statistics, see Table S1.

mitochondria (measured from the surface) to the AZ membrane, which was comparable between P10 (0.25 $\pm$ 0.15 μm) and P21 (0.29 $\pm$ 0.15 μm; Figure 1E).

To gain a more detailed insight into the CM structure, we analyzed the surface area of mitochondrial cristae. The surface area and density of CMs as well as their lamellar organization were shown to correlate with respiratory and ATP generating capacity of mitochondria.[41,42] Thus, changes in these parameters might hint to altered energy demands at AZs. Higher magnifications of Figures 1A and 1B are shown in Figures 1F and 1G in which the CMs were segmented. Notably, only in a subset of mitochondria CMs could be segmented, possibly due to the individual tilting direction, which is not ideal for every orientation of mitochondria within one tomogram due to the missing wedge. In this slightly lower number of mitochondria, where we also determined the mitochondrial volume separately, the difference in mitochondrial volume did not reach statistical significance (p = 0.0577; Figure 1H). Although we observed a significant increase in CM surface area from P10 (0.23 $\pm$ 0.15 μm^2) to P21 (0.30 $\pm$ 0.15 μm^2; p = 0.0424; Figure 1I) at non-endbulb synapses, the CM density was comparable between prehearing (28.66 $\pm$ 5.13 μm^{-1}) and young hearing mice (30.42 $\pm$ 5.95 μm^{-1}; p = 0.2782; Figure 1J). Finally, the cristae of mitochondria of P10 non-endbulb synapses were found to be shaped similarly to those of P21 synapses as shown by the comparable crista shape factor (CM surface area/CM lumen volume; Figure 1K).

Taken together, mitochondria at non-endbulb synapses tended to increase in volume and had greater CM surface areas upon maturation. All values and statistical details can be found in Table S1.

Mitochondrial occupation of presynapses increases during the development of the anteroventral cochlear nucleus

So far, we used for our analysis HPF/FS in combination with electron tomography. As mentioned above, this method has the limitation of only being able to visualize a proportion of mitochondria. To overcome this limitation, we made use of focused ion beam-scanning electron microscopy (FIB-SEM) on wt mice. This allowed for the reconstruction of larger volumes, but with a lower resolution, and therefore is complementary to our tomography analysis. We analyzed non-endbulb synapses that we could fully capture in our FIB-SEM datasets with the required resolution to also investigate the CM structure upon development. This further allowed us to ask, whether all presynaptic boutons harbored mitochondria, a question that we could not approach with electron-tomography. We generated scans from two wt age groups, P9 prior to hearing onset and P20 after the hearing onset. The datasets (2 for each age) contained a 3D volume reconstruction within the AVCN.

We analyzed excitatory presynapses of small bouton-like terminals from P9 and P20 respectively (Figures 2A and 2B). As for tomography, the synapses were identified via the presence of a PSD and a clear presynaptic SV cluster. Furthermore, we selected only boutons that were completely imaged. First, all visible terminals were inspected for the abundance of presynaptic mitochondria. For the mitochondrial occupation of presynapses, we did not consider mitochondria located in the axon. For the P9 animal, we found 222 presynapses of which 121 presynapses were occupied with mitochondria. For the P20 animal, we found in total 162 presynapses of which 130 presynapses were occupied with mitochondria. On average 55.3% of presynapses in the immature animal contained mitochondria at presynaptic sites with a significant increase of mitochondrial occupation to 80% on average during maturation in the P20 animal (p = 0.0079; Figure 2C).

The structure of presynaptic boutons changes during the development of the anteroventral cochlear nucleus

Next, we analyzed presynaptic boutons in the two imaged age groups in more detail and determined their volume as well as the number of SVs alongside with the PSD size. We used IMOD[43] to create segmentations of the presynaptic boutons, SVs, PSDs and presynaptic mitochondria (visualized in Figures 2A and 2B). For the analysis of the P9 animal, we selected a total of 20 boutons (10 per imaged stack) without presynaptic mitochondria as well as 20 boutons (10 per imaged stack) containing presynaptic mitochondria. We found an average volume of 0.55 $\pm$ 0.25 μm^3 of boutons without mitochondria. Boutons containing presynaptic mitochondria were significantly larger with an average size of 1.27 $\pm$ 1.07 μm^3 (p = 0.0011) (Figure 2D). The size of the PSD measured 0.005 $\pm$ 0.004 μm^3 on average in P9 boutons without presynaptic mitochondria and with presynaptic mitochondria showed a slightly increased average volume of the PSDs of 0.007 $\pm$ 0.005 μm^3 (Figure 2E). However, these differences did not reach statistical significance (p = 0.1612). P9 boutons without mitochondria had on average 364 $\pm$ 146 SVs, while P9 boutons containing presynaptic mitochondria harbored 639 $\pm$ 574 SVs, but this increase did not reach statistical significance (p = 0.0615) (Figure 2F). For the analysis of the P20 animal, we could select a total of 15 boutons (10 in the first dataset and 5 in the second dataset) without presynaptic mitochondria as well as 15 boutons (10 in the first dataset and 5 in the second dataset) containing presynaptic mitochondria. P20 boutons without presynaptic mitochondria had an average size of 1.20 $\pm$ 1.02 μm^3. P20 boutons containing presynaptic mitochondria had a size of 2.95 $\pm$ 2.48 μm^3 on average making them significantly larger compared to P20 boutons without mitochondria (p = 0.0222) and P9 boutons containing presynaptic mitochondria (p = 0.0409; Figure 2D). The size of PSDs in P20 boutons without mitochondria measured 0.012 $\pm$ 0.015 μm^3, while P20 boutons with mitochondria showed a trend toward larger PSDs (0.011 $\pm$ 0.007 μm^3; p = 0.4994) compared to P20 boutons without mitochondria (Figure 2E). For P20 boutons without mitochondria we determined a number of 483 $\pm$ 299 SVs. In
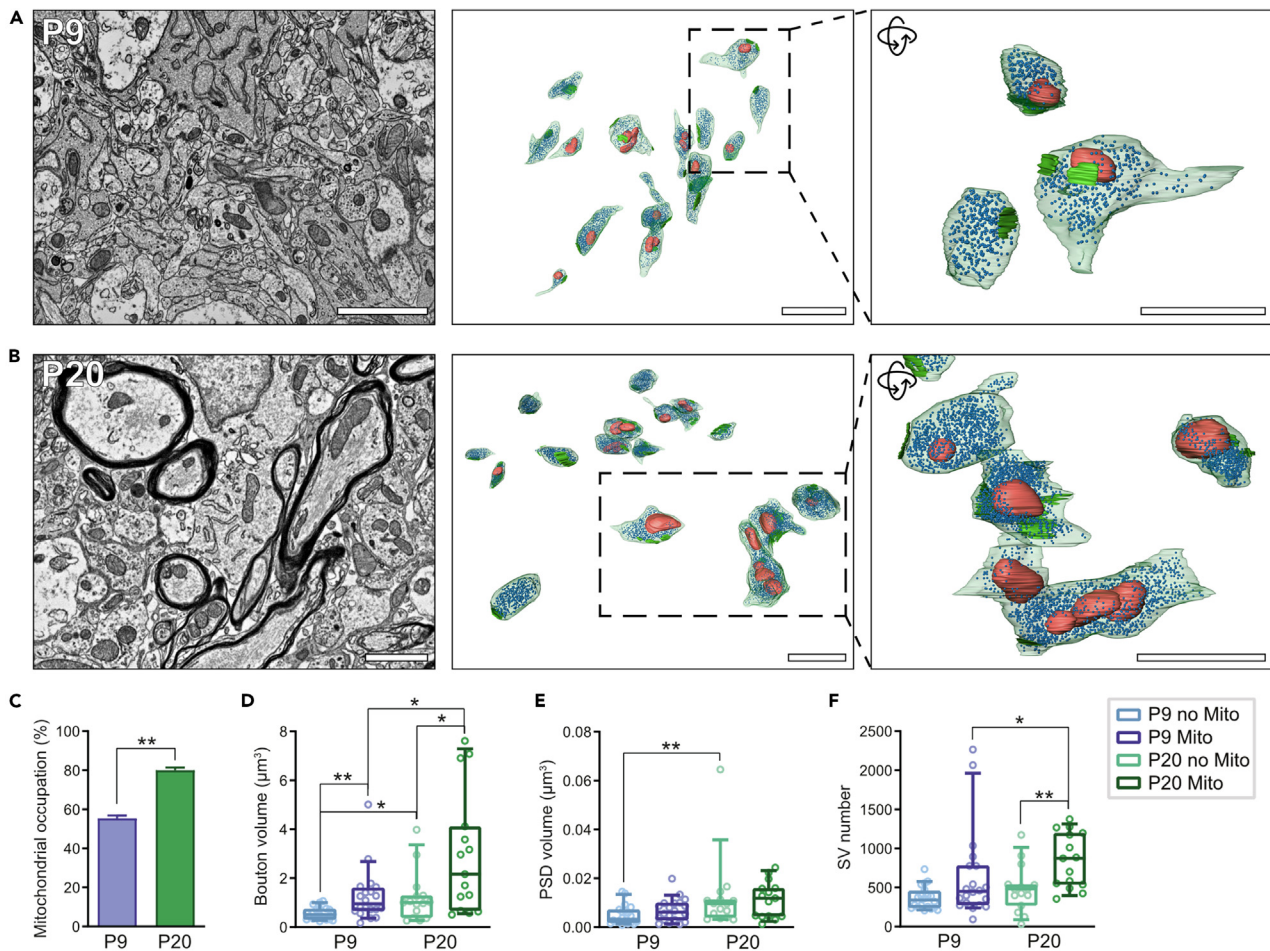
Figure 2. Bouton morphology and mitochondrial occupation of presynapses upon maturation

(A) Left: Example FIB-SEM image of a P9 animal that was used for segmentation. Middle: Overview of segmented boutons of one P9 animal. Light green: bouton membrane; blue: synaptic vesicles; red: mitochondria; green: postsynaptic density. Right: Detailed view of selected boutons in the dashed box. Scale bars 2 μm.

(B) Left: Example FIB-SEM image of a P20 animal that was used for segmentation. Middle: Overview of segmented boutons of one P20 animal. Light green: bouton membrane; blue: synaptic vesicles; red: mitochondria; green: postsynaptic density. Right: Detailed view of selected boutons in the dashed box. Scale bars 2 μm.

(C) Mitochondrial occupation of presynapses is significantly increased from P9 (55%) to P20 (80%) (p = 0.0079).

(D) The bouton volume increases from P9 to P20 and is significantly higher at presynapses containing a mitochondrion at both ages.

(E) The PSD volume increases significantly upon hearing onset at presynapses without a mitochondrion (p = 0.0052).

(F) After the onset of hearing, presynaptic boutons containing mitochondria exhibit larger SV pools compared to presynaptic boutons without mitochondria (p = 0.0049) and compared to presynaptic boutons at P9 (p = 0.0150). Bar graphs in C present average + SEM. Box and whisker plots in D–F present median, lower/upper quartiles, and 10-90th percentiles. P9: N = 1 animal, n = 2 dataset/image stack, P20: N = 1 animal, n = 2 dataset/image stack. *p < 0.05; **p < 0.01. For values and statistics, see Table S2.

comparison, P20 boutons containing presynaptic mitochondria showed a significant increase in the average number of SVs with 846 ± 350 SVs compared to P20 boutons without mitochondria (p = 0.0049) and P9 boutons containing presynaptic mitochondria (p = 0.0150; Figure 2F).

The increase in size of presynaptic structures at P20 suggests a higher synaptic activity that is enabled by larger boutons that harbor larger numbers of SVs and larger mitochondria. The trend toward larger PSD volumes further supports the argument for more synaptic transmission after the onset of hearing. However, to understand the structural adaptation of mitochondria to an increase in presynaptic energy demand a detailed analysis of the inner mitochondrial membranes is needed.

Structural remodeling of presynaptic mitochondria upon development

We analyzed the structure of presynaptic mitochondria at both developmental stages (P9 and P20; Figure 3). At both ages, we selected presynaptic mitochondria that showed no sign of osmotic perturbations such as crista swelling or major outer membrane irregularities that might be a result of chemical fixation and resin embedding (Figure S3). We performed manual segmentation of the outer mitochondrial membrane
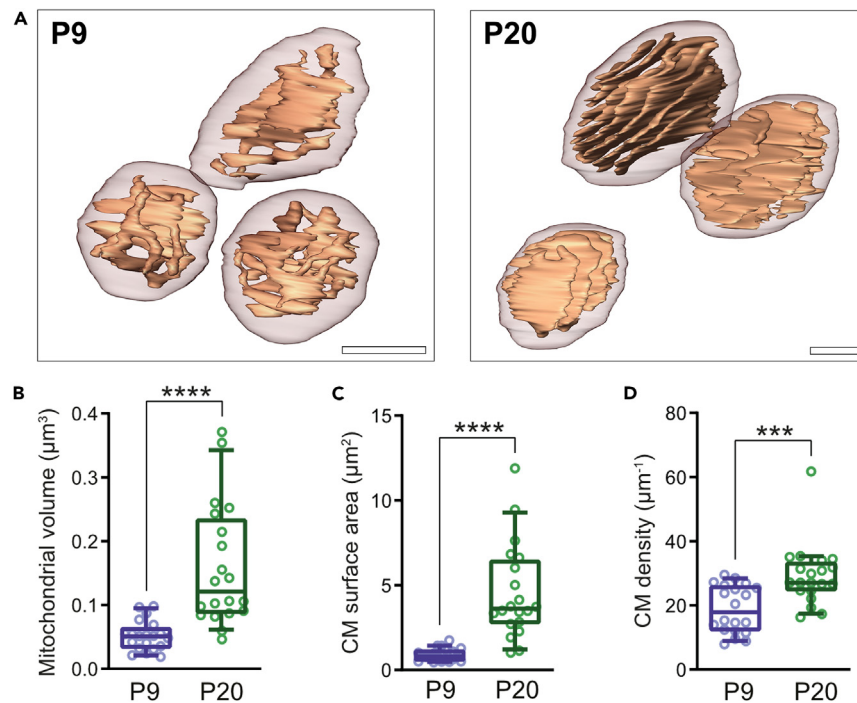
Figure 3. Structural changes of mitochondria morphology after hearing onset

(A) 3D models of presynaptic mitochondria at P9 before the onset of hearing and at P20 (red: mitochondrial outer membrane: orange: crista membranes (CM)). Presynaptic mitochondria at P9 exhibit crista membranes with irregular shape. Presynaptic mitochondria at P20 exhibit large crista membranes with regular shape. Scale bars 200 nm.

(B) Box and whiskers plot of mitochondrial volumes demonstrates a significant higher volume of mitochondria in presynaptic boutons at P20 (p < 0.0001).

(C) Box and whiskers plot of crista membrane surface areas shows a significantly larger CM surface area for mitochondria in presynaptic boutons at P20 (p < 0.0001).

(D) Box and whiskers plot of the crista membrane densities demonstrating a significantly higher CM density in presynaptic mitochondria at P20 (p = 0.0002). Box and whisker plots in B–D present median, lower/upper quartiles, and 10-90th percentiles. ***p < 0.001; ****p < 0.0001. For values and statistics, see Table S2.

and CMs of the same mitochondria. In total, we analyzed 20 presynaptic mitochondria in the P9 animal (10 mitochondria per dataset) and 20 presynaptic mitochondria in the P20 animal (12 mitochondria in the first dataset and 8 mitochondria in the second dataset; Figure 3A). In presynaptic mitochondria at P9, we found an average mitochondrial volume of 0.05 ± 0.02 μm^3. At P20, mitochondria revealed a significantly higher average mitochondrial volume of 0.16 $\mu m^3 \pm 0.09$ μm^3 (p < 0.0001; Figure 3B). At P9, we found an average CM surface area of 0.88 ± 0.38 μm^2 in mitochondria and a significantly larger CM surface area of 4.54 ± 2.79 μm^2 for P20 mitochondria (p < 0.0001; Figure 3C).

Next, we determined the CM density that corresponds to the ratio of the crista surface area normalized to the mitochondrial volume, which gives more information about the packing density of the CMs. We found an average of 18.85 ± 7.42 μm^{-1} in presynaptic mitochondria at P9. The CM density of mitochondria in P20 synapses with 29.16 ± 9.53 μm^{-1} on average was also significantly increased compared to presynaptic mitochondria at P9 (p = 0.0002; Figure 3D). These results suggest not only an increased mitochondrial size to meet higher presynaptic energy demands but additionally a specific adaptation of the crista architecture to potentially elevate mitochondrial respiration after the onset of hearing.

In conclusion, after onset of hearing we found clear morphological changes of mitochondria in bouton-like synapses of the AVCN. The number of synaptic boutons with mitochondria increased. Such boutons were also larger and capable to harbor more SVs. Furthermore, the mitochondria increased in volume accompanied with a higher CM density, which could point toward a more efficient energy production.

Mitochondria are larger at non-endbulb synapses compared to endbulb active zones of P10 mice

Next, we compared mitochondrial parameters between the specialized endbulb of Held synapses and non-endbulb synapses before and after the onset of hearing to test, whether changes in mitochondrial morphology upon hearing onset are a more general feature within the AVCN. Endbulbs of Held harbor, compared to smaller, bouton-like terminals, several specificities. The terminals comprise hundreds of individual AZs and mitochondria are highly abundant.[44,45] FIB-SEM permits to investigate a larger number of small bouton-like terminals but might not deliver an appropriate number of endbulb terminals due to a limitation in the total volume of the image stack. Thus, we used electron tomography after HPF/FS for these experiments, which additionally reaches the highest possible resolution also on the cristae structure. The selection of terminals was done as described above and an example endbulb of Held from a P10 wt mouse is depicted in Figure S1.
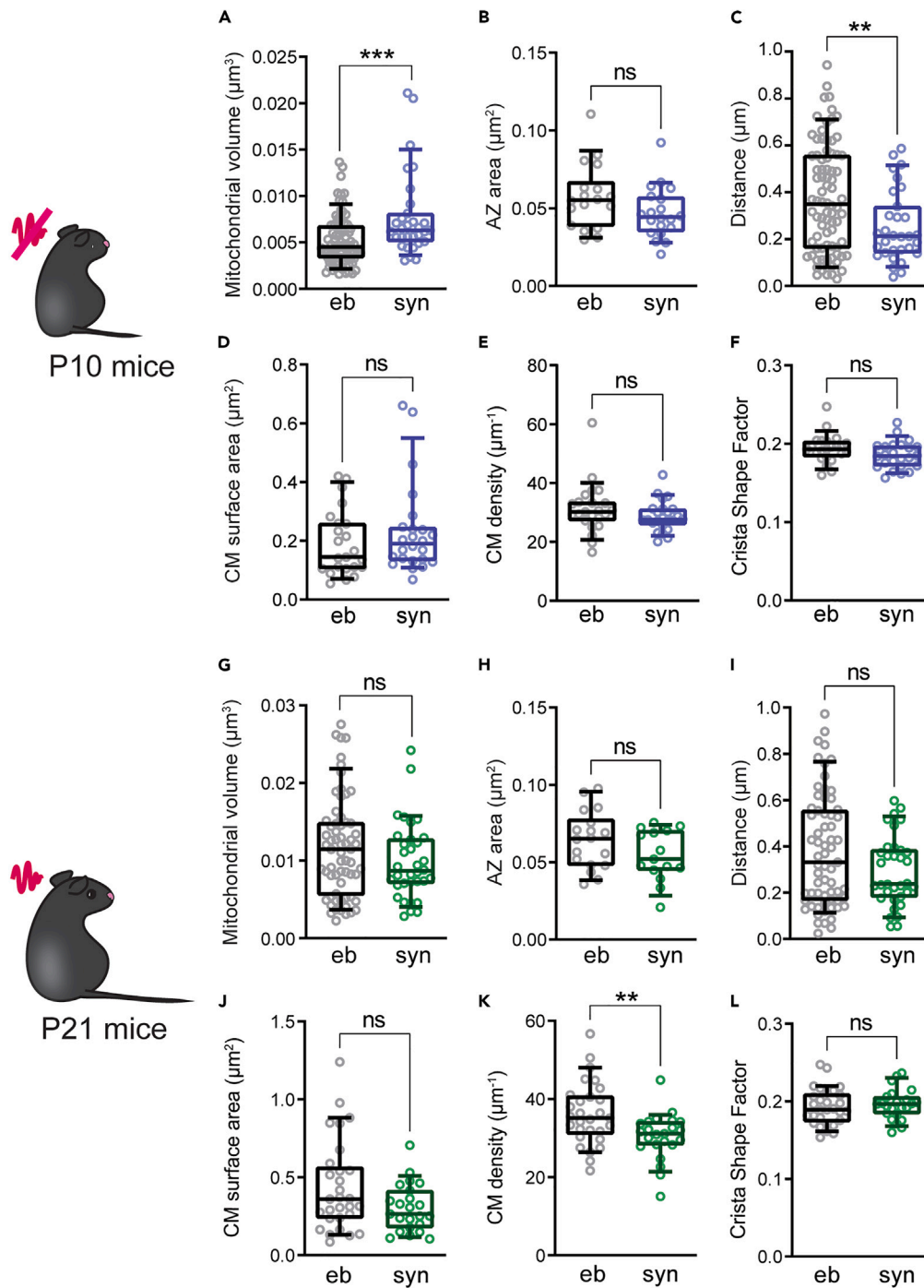
Figure 4. Presynaptic mitochondria in non-endbulb and endbulb synapses from wt mice before and after the hearing onset

(A and G) Considering all analyzed mitochondria, their volumes are larger at non-endbulb synapses (abbreviated as syn) compared to endbulbs (eb) at pre-hearing mice (p = 0.0079) (A), while they are comparable between both synapse types at P21 (G).

(B and H) The reconstructed AZ areas are similar between the synapse types at both time points.

(C and I) The shortest distance of the mitochondria to the AZ membrane is higher at endbulb synapses before the onset of hearing (p = 0.0079) (C) The difference is not significant at P21 (I).

(D and J) The sum of the CM surface areas is comparable between mitochondria of both groups.

(E and K) The CM density (CM surface area/mitochondrial volume) is comparable between the synapse types at the age of P10 (E) while it is higher in endbulb mitochondria at P21 (p = 0.0079) (K).

Figure 4. Continued

(F and L) The crista shape factor (CM surface area/CM lumen volume) is the same between mitochondria of the two groups at both ages. Box and whisker plots present median, lower/upper quartiles, 10–90th percentiles. ns, not significant; **p < 0.01; ***p < 0.001. eb P10 (N = 3; n = 82/23) in black and syn P10 (N = 3; n = 31/24) in blue. (N: number of animals; n: number of mitochondria (all/with the segmentation of cristae). For values and statistics, see Tables S3 and S4. The datasets of the non-endbulb synapses are the same as in Figure 1.

Please note that the non-endbulb datasets depicted in Figure 1 are now compared to endbulb of Held datasets. We found that at the pre-hearing stage, average mitochondrial volumes were greater at non-endbulb synapses (0.008 ± 0.005 μm^3) compared to mitochondria within endbulb terminals (0.005 ± 0.003; p = 0.0007; Figure 4A). AZ areas of endbulb terminals measured on average 0.057 ± 0.021 μm^2 and tended to be larger compared to non-endbulb synapses (0.047 ± 0.017 μm^2), but the difference did not reach statistical significance (p = 0.0987; Figure 4B). The mean shortest distance of mitochondria to the AZ membrane was significantly higher at endbulbs (0.37 ± 0.23 μm) compared to non-endbulb terminals (0.25 ± 0.15 μm; p = 0.0018; Figure 4C), which might simply be an effect of spatial constrains in non-endbulb terminals which in general are smaller compared to endbulb terminals.

For completeness, we also determined the volumes of the subgroup of mitochondria with reconstructed CMs (see explanation above). Non-endbulb mitochondria showed only a trend to increased volumes compared to endbulb terminals at the age of P10 (p = 0.0772; Figure S4A; Table S3). However, at P21 the mean volume of this subgroup of mitochondria tended to be higher in endbulb terminals (p = 0.3747; Figure S4B; Tables S3 and S4). The surface area of the cristae (p = 0.2806; Figure 4D) as well as their density (p = 0.1681; Figure 4E) was found to be comparable between endbulb and non-endbulb mitochondria at P10. Moreover, the crista shape factor was also similar between both synapse types (p = 0.0972; Figure 4F). All values and statistics are listed in Table S3. In conclusion, non-endbulb and endbulb mitochondria in the pre-hearing stage resembled each other in shape with endbulb mitochondria being slightly, but significantly smaller in volume.

Mitochondria at endbulb synapses display a higher crista membrane density after the onset of hearing

At P21 mice, mitochondrial volumes (p = 0.2034; Figure 4G), AZ areas (p = 0.1221; Figure 4H) and the shortest distance of mitochondria to the AZ membrane (p = 0.1983; Figure 4I) were comparable at endbulb and non-endbulb terminals. Mitochondria with segmented CMs revealed similar volumes comparing endbulb (0.012 ± 0.006 μm^3) and non-endbulb synapses (0.010 ± 0.006; p = 0.3747 μm^3; Figure S4B), which points toward a high robustness of the data. The CM surface area was also comparable between mitochondria in endbulbs of Held (0.44 ± 0.29 μm^2) and non-endbulb mitochondria (0.30 ± 0.15 μm^2; p = 0.1115; Figure 4J). However, the CM density was found to be significantly higher at mitochondria of endbulb terminals (36.16 ± 7.99 μm^{-1}) vs. non-endbulb terminals (30.42 ± 5.95 μm^{-1}; p = 0.0046; Figure 4K) after hearing onset, hinting toward a specific need in these terminals for a high energy demand. The crista shape factor revealed that the cristae were similar in their organization (p = 0.6241; Figure 4L). All values and statistics can be found in Table S4.

We conclude that mitochondria in wt endbulb and non-endbulb synapses are largely comparable in size and morphology shortly after hearing onset but a higher CM density might be needed in endbulbs of Held.

Presynaptic mitochondria are larger after the onset of hearing at endbulbs of Held but remain largely unchanged without auditory input

Next, we ask, whether auditory input in general alters mitochondrial volume as well as CM density and shape. We chose endbulb synapses for our analysis because here auditory information is directly processed for further interpretation and included another age-group of 6-month-old mice (6M) to determine changes toward adulthood. Moreover, we compared our wt results to otoferlin lacking endbulb of Held terminals with comparable ages of P10, P22 mice and 6M (Figure 5A). $Otof^{-/-}$ mice are congenitally deaf, therefore, these animals did not experience any auditory triggered activity, and endbulb AZs revealed significantly fewer SVs upon development.[31]

The comparison of all analyzed mitochondria (Figure S5A) revealed that mitochondria had significantly larger volumes at endbulbs of young hearing wt mice (0.012 ± 0.006 μm^3) compared to pre-hearing mice (0.005 ± 0.003 μm^3; p < 0.0001; Figure S5A). During further development toward adulthood, mitochondria continued to increase in volume (0.027 ± 0.017 μm^3; Figure S5A). In contrast, in $Otof^{-/-}$ mice, mitochondria also increased in volume toward adulthood, but to a much smaller extent. In the pre-hearing stage, mitochondria were even bigger in $Otof^{-/-}$ mice (0.009 ± 0.006 μm^3; p < 0.0001) compared to wt but already shortly after the onset of hearing, mitochondria showed smaller volumes in the deaf animals (0.009 ± 0.006 μm^3; p = 0.0066). This difference was most obvious comparing adult wt and $Otof^{-/-}$ mice (0.014 ± 0.010 μm^3; p < 0.0001; Figure S5A). The AZ areas at endbulbs were comparable between the age groups in wt and $Otof^{-/-}$ animals (Figure S5B), which is consistent with previous findings (Hintze et al., 2021). However, AZ areas were found to be significantly smaller in the $Otof^{-/-}$ (0.049 ± 0.014 μm^2) compared to wt mice (0.064 ± 0.019 μm^2; p = 0.0048; Figure S5B) at the age of P22.

Next, we determined the mean shortest distance of the reconstructed mitochondria to the AZ. As pointed out above, a closer distance could correlate with a higher and more reliable ATP supply that is particularly important to maintain SV release upon stimulation,[46] but might also regulate Ca^{2+} concentrations directly at the AZ. The distances of mitochondria to the AZ membrane were highly variable in endbulb terminals but not significantly different between the age groups and genotypes (Figure S5C), reflecting that the mitochondria were found in the whole endbulb terminal without an obvious accumulation in a specific area. The comparison of the reconstructed volumes of the subset of mitochondria with segmented CMs were similar to the comparison of all mitochondria. Still, we observed a significant increase in mitochondrial volumes throughout development in wt and $Otof^{-/-}$ (Figures 5B and S5D) with the most prominent difference between wt and $Otof^{-/-}$ in adult animals (Figure S5D). The surface area of the CMs was also significantly greater at endbulb mitochondria of the young hearing mice
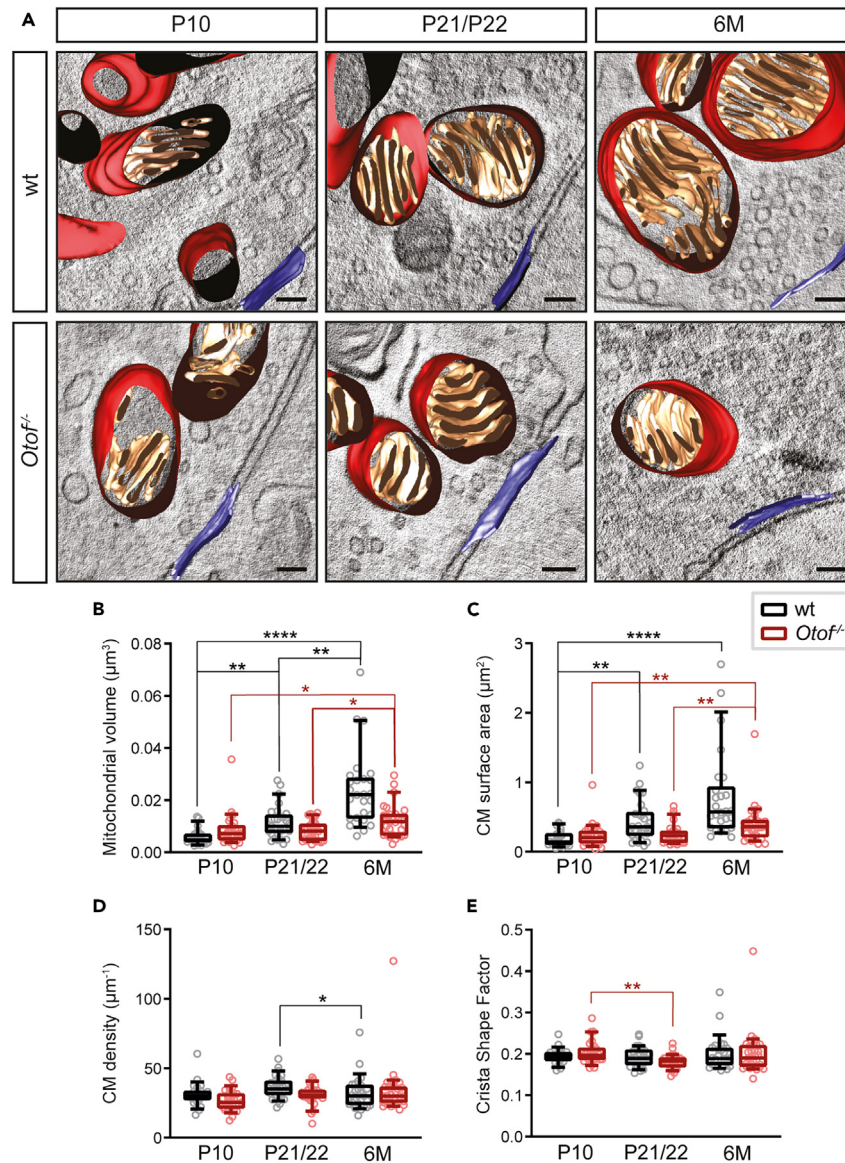
Figure 5. Auditory input influences size and shape of mitochondria in endbulb synapses

(A) 3D model with the z-view of a tomogram showing AZ membranes (blue) and presynaptic mitochondria (red) with cristae (beige) within an endbulb terminal of a P10 and a P21/22 and 6M wt and $Otof^{-/-}$ mouse. Scale bars 100 nm.

(B) The volume of the mitochondria in which the CMs could be reconstructed increases markedly upon development in wt and slightly in $Otof^{-/-}$ endbulbs.

(C) The sum of surface areas of CMs increases upon development in wt and $Otof^{-/-}$ endbulb mitochondria.

(D) The CM density (CM surface area/mitochondrial volume) decreases from P21 to 6M in wt while it is unchanged in $Otof^{-/-}$ mice during development.

(E) The crista shape factor (CM surface area/CM lumen volume) indicates no change in the organization of the cristae in wt, but points to more tubular shaped cristae at P22 compared to P10 in $Otof^{-/-}$ mice. Box and whisker plots present median, lower/upper quartiles, 10–90th percentiles. ns, not significant; *p < 0.05; ***p < 0.001, ****p < 0.0001. wt P10 (N = 3; n = 82/23), wt P21 (N = 3; n = 65/29), wt 6M (N = 3; n = 40/26) in black. $Otof^{-/-}$ P10 (N = 3; n = 48/27), $Otof^{-/-}$ P22 (N = 3; n = 67/29), $Otof^{-/-}$ 6M (N = 3; n = 52/29) in red. (N: number of animals; n: number of mitochondria (all/with the segmentation of CMs). For simplicity, we here depict only the significances between the age groups. All significances and comparisons applied between the genotypes are shown in Figure S3 and details about values and statistics can be found in Tables S5–S9. The datasets of the P10 and P21 wt endbulbs are the same as in Figure 4.

(0.44 ± 0.29 μm^2) compared to pre-hearing mice (0.19 ± 0.11 μm^2) and increased toward adulthood in wt (0.79 ± 0.64 μm^2; Figures 5C and S5E). In $Otof^{-/-}$ mice, the CM surface areas were comparable between P10 (0.24 ± 0.18 μm^2) and P22 (0.25 ± 0.15 μm^2), but increased toward adulthood (0.41 ± 0.29 μm^2; Figures 5C and S5E). The ratio of CM surface area and mitochondrial volume, which represents the CM density, slightly increased throughout development in wt with a significant difference comparing P21 (36.16 ± 7.99 μm^{-1}) and 6M (31.99 ± 12.22 μm^{-1}; p = 0.0492; Figures 5D and S5F), while in $Otof^{-/-}$ mice, CM densities were comparable between the age groups. Strikingly,
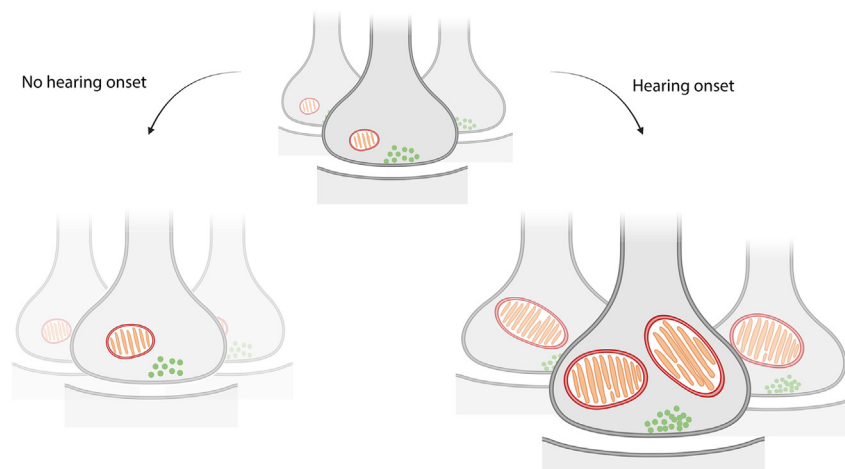
Figure 6. Changes of mitochondrial volume and CMs synaptic terminals upon development and deafness

Prior to hearing onset endbulb and non-endbulb synapses exhibit smaller mitochondria compared to after hearing onset. In hearing animals, the mitochondria tend to enlarge upon further maturation toward adulthood as shown for endbulb terminals. On the other hand, without auditory input in congenitally deaf animals, mitochondria remain rather small. Illustration created with BioRender.com.

when comparing genotypes, we found significant differences at P10 (p = 0.0412) and P21/22 (p = 0.0210) but not in the adult groups (Figure S5F). The crista shape factor that describes the lamellarity of cristae appeared similar in all wt age groups (Figure 5D). In deaf animals, the crista shape factor decreased from P10 (0.20 ± 0.03) to P22 (0.18 ± 0.02; p = 0.0039; Figure 5D), while the other groups did not differ significantly. Comparing genotypes, we only found a significant difference in the P21/P22 group, indicating that CMs are less lamellar, but more tubular shaped in the $Otof^{-/-}$ P22 group (Figure S5G). Therefore, maturation but also the lack of auditory input causes structural changes of mitochondria. All values and statistics can be found in Tables S5–S9.

To sum up, we found significantly more mitochondria occupied non-endbulb synapses in the AVCN after hearing onset (summarized in Figure 6). These synapses further harbored more SVs, likely due to the increased bouton size. The mitochondria at non-endbulb synapses as well as in endbulb synapses increased in size upon hearing onset. Notably, for non-endbulb synapses this trend was not significant. In the pre-hearing age, mitochondria were larger at non-endbulb synapses compared to endbulbs. However, the distinct developmental increase in mitochondrial volumes at endbulb terminals and the only slight increase at non-endbulb synapses resulted in comparable mitochondrial volumes at P21. Overall, the distances between mitochondria and the nearest AZ membrane were comparable between P10 and P21 at both, endbulb and non-endbulb synapses. The distances at non-endbulb synapses were significantly smaller at P10, which could be a result of smaller sized non-endbulb terminals. Consistent with the larger mitochondrial volumes after the onset of hearing, the surface area of cristae also increased during maturation at endbulb and non-endbulb synapses, while the CM density was only increased at mitochondria of non-endbulb synapses according to the FIB-SEM data, which show reliably the full mitochondrial volume. The surface area and density of CMs were comparable between the synapse types at P10, while the CM density was larger at mitochondria of endbulbs compared to non-endbulbs at P21 despite a comparable mitochondrial volume and CM surface area. These differences resulted from the pronounced increase in the surface area of cristae during maturation at endbulbs, whereas at mitochondria at non-endbulb synapses only a slight increase the CM surface area was observed. The crista shape factor was found to be similar in all age groups, suggesting that the shape of CMs was not significantly affected by the maturation process and comparable between mitochondria of different excitatory synapses within the AVCN. However, some differences in the CM density were observable in the FIB-SEM data. Finally, in deaf animals the increase in mitochondrial volume from pre-hearing toward 6-month-old animals was visible but to a much lower extent compared to wt, the same accounted for the CM surface. Therefore, we conclude that auditory input significantly influences the size of mitochondria and to a certain extent also the CM density. Thus, the enlargement of mitochondria likely correlated to higher energy demands in the AVCN of hearing mice.

DISCUSSION

Mitochondrial occupation of anteroventral cochlear nucleus synapses

Mitochondria were observed to be anchored in nerve terminals near AZs from various CNS regions including the hippocampus,[47] the thalamic nuclei[48] as well as the auditory brainstem.[27,36,38,40,49] It has been reported that the presence of presynaptic mitochondria at axonal AZs positively correlates with the size of synapses, the SV density and the SV release,[15,46] similar to what we found for non-endbulb synapses within the AVCN. In addition, the mobilization of reserve pool SVs has been demonstrated to be disturbed at synapses that lack mitochondria due to an insufficient ATP supply,[1] speaking for a high benefit in energy supply for AZs with mitochondria nearby. However, only half of hippocampal and cortical synapses harbor a mitochondrion,[15,50,51] which we also found in AVCN non-endbulb synapses prior to hearing onset. The initial

occupation of ~50% increased upon hearing onset to as much as 80%. Additionally, our data further indicate that endbulbs of Held always harbor a large number of mitochondria, which were in comparable distances to AZs in wt throughout development toward adulthood. Mitochondria seemed not to disappear from endbulb terminals in deaf animals though they were smaller in comparison to age-matched controls. Therefore, in the fully functional AVCN, the high energy demand appears to be satisfied, at least in part, by a high mitochondrial occupation of the synapses.

The structure of mitochondria changes upon different energy demands

In addition to the presence or absence of mitochondria, different needs for energy might translate in a change of mitochondrial size. In endbulbs from cats, the average mitochondrial size did not change, but a steady increase in mitochondrial volume fraction was observed until 60 days of age.[52] Moreover, Ryugo and colleagues estimated in an earlier study that endbulbs from high spontaneous rate fibers contained 50% greater mitochondria compared to endbulbs from low spontaneous rate fibers.[45] In the calyx of Held and minor terminals contacting the principal cells, maturation from pre-hearing to hearing was associated with an increase in mitochondrial volume.[14] In line with these observations, we found larger volumes of the reconstructed mitochondria for non-endbulb synapses and endbulbs of Held after hearing onset. Of note, the literature describes several smaller inputs from various sources on spherical BCs including small bouton-like inputs from auditory nerve fibers (ANFs) and inputs from other parts of the CN (reviewed in ref.[53]). We cannot determine the connectivity with the methods used in our study, but it was described that not just ANFs, but also intrinsic connections within the CN follow the tonotopic organization.[54] Furthermore, bouton-like synapses coming from the auditory nerve that contact SBC dendrites seem to modulate auditory processing by enhancing the temporal precision and fidelity.[33] Thus, it is conceivable that also the non-endbulb synapses analyzed in our study depend on the activity of the auditory system. We could clearly show that both, wt non-endbulb and endbulb synapses, harbor larger mitochondria upon hearing onset, while deaf $Otof^{-/-}$ mice revealed only a shallow increase in mitochondrial volume in endbulbs of Held compared to wt animals. Recently it has been described for *Drosophila* larval neuromuscular junctions that terminals with highest energy demands have the greatest mitochondrial size together with a higher packing density of mitochondria.[55] Thus, we propose that the enlarged mitochondria in young hearing and adult wt AVCN are rather an adaptation to high energy demands and not a sign of malfunction. An increase in mitochondrial size and cristae surface area from pre-hearing to young mice is not visible in $Otof^{-/-}$ endbulb synapses, possibly due to the strikingly reduced frequency of spontaneous miniature events found in spiral ganglion neurons of P9 otoferlin lacking mice.[56] Furthermore, we suggest that the substantial decline in the SV density in adult $Otof^{-/-}$ endbulb synapses[31] significantly lowers the need for ATP since Pulido and Ryan could show that SVs represent the main source of energy consumption in synaptic terminals.[57]

Developmental maturation is associated with ultrastructural remodeling of mitochondria in the anteroventral cochlear nucleus

Cristae are described as pleomorphic membranes, ranging from tubular structures to sheet-like lamellae and it was proposed that tubular cristae merge to form large lamellae.[58] A lamellar CM arrangement seems to be beneficial for high-performance mitochondria as it has been shown for the hippocampus.[12] In our study, we used FIB-SEM on fixed material with a lateral pixel size of 2 nm and z of 5 nm as well as electron tomography on near-to-native cryofixed samples with a pixel size of 1.2–1.7 nm (dependent on the magnification we used for the tomogram recording). Both methods allowed to visualize and segment CMs and were shown to result in comparable quality of mitochondrial morphology.[59] Notably, Perkins et al. found that the inner architecture of cryofixed mitochondria in brown adipocytes was similar to that of chemically fixed mitochondria, but crista volumes were more sensitive to chemical fixation than the surface area.[60]

To our surprise, we only found slight morphological changes of the CM morphology upon hearing onset. Our FIB-SEM data revealed a higher CM density, but only mild changes in the CM structure could be observed in our HPF/FS samples for both non-endbulb and endbulb mitochondria. The decrease in the crista shape factor from P10 to P22 in the $Otof^{-/-}$ mice might indicate less lamellar CMs in the P22 $Otof^{-/-}$, but we mainly observed differences in mitochondrial volume and CM surface area comparing adult wt and $Otof^{-/-}$ as well as comparing the different age groups. In summary, our experiments point to a change in CMs area and density upon activity changes together with an increase in mitochondrial volume.

Limitations of the study

Using electron tomography of mitochondria generated from 250-nm semithin sections together with HPF/FS harbors some limitations. First, the required acute slice preparation of the AVCN might influence sample quality, the tissue preservation might be altered due to differences in the preparation time or even prolonged preparation. Combining electron tomography and HPF/FS in general provides an excellent tissue preservation enabling a resolution in 3D in a 1.5 nm range. However, mitochondria are structures exceeding this dimension and the capability to depict entire a full 3D reconstruction using electron tomography is limited. Despite these limitations, the large number of reconstructed mitochondria plus sampling them over different areas and from different animals results in robust differences in the size of the depicted proportions of the mitochondria. Our FIB-SEM data match these findings but rely on a low number of replica. Thus, we only take them as a support for the tomography results. Finally, the clear origin of non-endbulb, bouton-like synapses cannot be determined in this study, neither using FIB-SEM nor electron tomography. 3D volume reconstructions of significantly larger volumes of the CN would be required to determine the connectivity, which exceeds the scope of this study.

STAR★METHODS

Detailed methods are provided in the online version of this paper and include the following:

SUPPLEMENTAL INFORMATION

Supplemental information can be found online at https://doi.org/10.1016/j.isci.2023.108700.

AUTHOR CONTRIBUTIONS

S.J. and C.W. designed the study. A.H. performed electron microscopic work (HPF/FS, enhanced *en bloc* stainings, electron tomography, preparation of samples for FIB-SEM). F.L. analyzed FIB-SEM datasets with the contribution of J.A. A.M.S. performed FIB-SEM with the contri-bution of W.M. A.H., F.L., S.J., and C.W. prepared the article with contributions from all other authors.

DECLARATION OF INTERESTS

The authors declare no conflict of interest.

REFERENCES

1. Verstreken, P., Ly, C.V., Venken, K.J.T., Koh, T.-W., Zhou, Y., and Bellen, H.J. (2005). Synaptic Mitochondria Are Critical for Mobilization of Reserve Pool Vesicles at Drosophila Neuromuscular Junctions. Neuron *47*, 365–378.

2. Medler, K., and Gleason, E.L. (2002). Mitochondrial Ca(2+) buffering regulates synaptic transmission between retinal amacrine cells. J. Neurophysiol. *87*, 1426–1439.

3. David, G., and Barrett, E.F. (2003). Mitochondrial Ca2+ uptake prevents desynchronization of quantal release and minimizes depletion during repetitive stimulation of mouse motor nerve terminals. J. Physiol. *548*, 425–438.

4. Jonas, E.A., Buchanan, J., and Kaczmarek, L.K. (1999). Prolonged activation of mitochondrial conductances during synaptic transmission. Science *286*, 1347–1350.

5. Billups, B., and Forsythe, I.D. (2002). Presynaptic Mitochondrial Calcium Sequestration Influences Transmission at Mammalian Central Synapses. J. Neurosci. *22*, 5840–5847.

6. Tang, Y., and Zucker, R.S. (1997). Mitochondrial involvement in post-tetanic potentiation of synaptic transmission. Neuron 18, 483–491.

7. Chandel, N.S. (2014). Mitochondria as signaling organelles. BMC Biol. 12, 34.

8. Friedman, J.R., and Nunnari, J. (2014). Mitochondrial form and function. Nature 505, 335–343.

9. Sjöstrand, F.S. (1953). Electron Microscopy of Mitochondria and Cytoplasmic Double Membranes: Ultra-Structure of Rod-shaped Mitochondria. Nature 171, 30–31.

10. Palade, G.E. (1952). The fine structure of mitochondria. Anat. Rec. 114, 427–451.

11. Rube, D.A., and van der Bliek, A.M. (2004). Mitochondrial morphology is dynamic and varied. Mol. Cell. Biochem. 256–257, 331–339.

12. Cserép, C., Pósfai, B., Schwarcz, A.D., and Dénes, Á. (2018). Mitochondrial Ultrastructure Is Coupled to Synaptic Performance at Axonal Release Sites. eNeuro 5. ENEURO.0390-17.2018.

13. Ivannikov, M.V., Sugimori, M., and Llinás, R.R. (2013). Synaptic vesicle exocytosis in hippocampal synaptosomes correlates directly with total mitochondrial volume. J. Mol. Neurosci. 49, 223–230.

14. Thomas, C.I., Keine, C., Okayama, S., Satterfield, R., Musgrove, M., Guerrero-Given, D., Kamasawa, N., and Young, S.M. (2019). Presynaptic Mitochondria Volume and Abundance Increase during Development of a High-Fidelity Synapse. J. Neurosci. 39, 7994–8012.

15. Smith, H.L., Bourne, J.N., Cao, G., Chirillo, M.A., Ostroff, L.E., Watson, D.J., and Harris, K.M. (2016). Mitochondrial support of persistent presynaptic vesicle mobilization with age-dependent synaptic growth after LTP. Elife 5, e15275.

16. Zeng, F.G., Oba, S., Garde, S., Sininger, Y., and Starr, A. (1999). Temporal and speech processing deficits in auditory neuropathy. Neuroreport 10, 3429–3435.

17. Mikaelian, D., and Ruben, R.J. (1965). Development of Hearing in the Normal Cba-J Mouse: Correlation of Physiological Observations with Behavioral Responses and with Cochlear Anatomy. Acta Otolaryngol. 59, 451–461.

18. Babola, T.A., Li, S., Gribizis, A., Lee, B.J., Issa, J.B., Wang, H.C., Crair, M.C., and Bergles, D.E. (2018). Homeostatic control of spontaneous activity in the developing auditory system. Neuron 99, 511–524.e5.

19. Sonntag, M., Englitz, B., Kopp-Scheinpflug, C., and Rübsamen, R. (2009). Early postnatal development of spontaneous and acoustically evoked discharge activity of principal cells of the medial nucleus of the trapezoid body: an in vivo study in mice. J. Neurosci. 29, 9510–9520.

20. Tritsch, N.X., Zhang, Y.-X., Ellis-Davies, G., and Bergles, D.E. (2010). ATP-induced morphological changes in supporting cells of the developing cochlea. Purinergic Signal. 6, 155–166.

21. Pangršič, T., Reisinger, E., and Moser, T. (2012). Otoferlin: a multi-C2 domain protein essential for hearing. Trends Neurosci. 35, 671–680.

22. Rodríguez-Ballesteros, M., Reynoso, R., Olarte, M., Villamar, M., Morera, C., Santarelli, R., Arslan, E., Medá, C., Curet, C., Völter, C., et al. (2008). A multicenter study on the prevalence and spectrum of mutations in the otoferlin gene (OTOF) in subjects with nonsyndromic hearing impairment and auditory neuropathy. Hum. Mutat. 29, 823–831.

23. Yasunaga, S., Grati, M., Cohen-Salmon, M., El-Amraoui, A., Mustapha, M., Salem, N., El-Zir, E., Loiselet, J., and Petit, C. (1999). A mutation in OTOF, encoding otoferlin, a FER-1-like protein, causes DFNB9, a nonsyndromic form of deafness. Nat. Genet. 21, 363–369.

24. Yasunaga, S., Grati, M., Chardenoux, S., Smith, T.N., Friedman, T.B., Lalwani, A.K., Wilcox, E.R., and Petit, C. (2000). OTOF Encodes Multiple Long and Short Isoforms: Genetic Evidence That the Long Ones Underlie Recessive Deafness DFNB9. Am. J. Hum. Genet. 67, 591–600.

25. Vona, B., Rad, A., and Reisinger, E. (2020). The Many Faces of DFNB9: Relating OTOF Variants to Hearing Impairment. Genes 11, 1411.

26. Roux, I., Safieddine, S., Nouvian, R., Grati, M., Simmler, M.-C., Bahloul, A., Perfettini, I., Le Gall, M., Rostaing, P., Hamard, G., et al. (2006). Otoferlin, Defective in a Human Deafness Form, Is Essential for Exocytosis at the Auditory Ribbon Synapse. Cell 127, 277–289.

27. Cant, N.B., and Morest, D.K. (1979). The bushy cells in the anteroventral cochlear nucleus of the cat. A study with the electron microscope. Neuroscience 4, 1925–1945.

28. Held, H. (1893). Die centrale gehörleitung. Arch Anat Physiol Anat Abt 17, 201–248.

29. Ryugo, D.K., and Fekete, D.M. (1982). Morphology of primary axosomatic endings in the anteroventral cochlear nucleus of the cat: A study of the endbulbs of Held. J. Comp. Neurol. 210, 239–257.

30. Wu, S.H., and Oertel, D. (1984). Intracellular injection with horseradish peroxidase of physiologically characterized stellate and bushy cells in slices of mouse anteroventral cochlear nucleus. J. Neurosci. 4, 1577–1588.

31. Hintze, A., Gültas, M., Semmelhack, E.A., and Wichmann, C. (2021). Ultrastructural maturation of the endbulb of Held active zones comparing wild-type and otoferlin-deficient mice. iScience 24, 102282.

32. Wright, S., Hwang, Y., and Oertel, D. (2014). Synaptic transmission between end bulbs of Held and bushy cells in the cochlear nucleus of mice with a mutation in Otoferlin. J. Neurophysiol. 112, 3173–3188.

33. Koert, E., and Kuenzel, T. (2021). Small dendritic synapses enhance temporal coding in a model of cochlear nucleus bushy cells. J. Neurophysiol. 125, 915–937.

34. Oertel, D. (2011). GluA4 sustains sensing of sounds through stable, speedy, sumptuous, spineless synapses. J. Physiol. 589, 4089–4090.

35. Lin, L., Campbell, J., Oertel, D., and Smith, P.H. (2022). Local targets of T-stellate cells in the ventral cochlear nucleus. J. Comp. Neurol. 530, 2820–2834.

36. Lauer, A.M., Connelly, C.J., Graham, H., and Ryugo, D.K. (2013). Morphological Characterization of Bushy Cells and Their Inputs in the Laboratory Mouse (Mus musculus) Anteroventral Cochlear Nucleus. PLoS One 8, e73308.

37. Tatsuoka, H., and Reese, T.S. (1989). New structural features of synapses in the anteroventral cochlear nucleus prepared by direct freezing and freeze-substitution. J. Comp. Neurol. 290, 343–357.

38. Rowland, K.C., Irby, N.K., and Spirou, G.A. (2000). Specialized synapse-associated structures within the calyx of Held. J. Neurosci. 20, 9135–9144.

39. Gray, E.G. (1963). Electron microscopy of presynaptic organelles of the spinal cord. J. Anat. 97, 101–106.

40. Tolbert, L.P., and Morest, D.K. (1982). The neuronal architecture of the anteroventral cochlear nucleus of the cat in the region of the cochlear nerve root: Golgi and Nissl methods. Neuroscience 7, 3013–3030.

41. Cogliati, S., Frezza, C., Soriano, M.E., Varanita, T., Quintana-Cabrera, R., Corrado, M., Cipolat, S., Costa, V., Casarin, A., Gomes, L.C., et al. (2013). Mitochondrial cristae shape determines respiratory chain supercomplexes assembly and respiratory efficiency. Cell 155, 160–171.

42. Song, D.H., Park, J., Maurer, L.L., Lu, W., Philbert, M.A., and Sastry, A.M. (2013). Biophysical significance of the inner mitochondrial membrane structure on the electrochemical potential of mitochondria. Phys. Rev. E - Stat. Nonlinear Soft Matter Phys. 88, 062723.

43. Kremer, J.R., Mastronarde, D.N., and McIntosh, J.R. (1996). Computer visualization of three-dimensional image data using IMOD. J. Struct. Biol. 116, 71–76.

44. Nicol, M.J., and Walmsley, B. (2002). Ultrastructural basis of synaptic transmission between endbulbs of Held and bushy cells in the rat cochlear nucleus. J. Physiol. 539, 713–723.

45. Ryugo, D.K., Wu, M.M., and Pongstaporn, T. (1996). Activity-related features of synapse morphology: A study of endbulbs of Held. J. Comp. Neurol. 365, 141–158.

46. Sun, T., Qiao, H., Pan, P.-Y., Chen, Y., and Sheng, Z.-H. (2013). Motile axonal mitochondria contribute to the variability of presynaptic strength. Cell Rep. 4, 413–419.

47. Spacek, J., and Harris, K.M. (1998). Three-dimensional organization of cell adhesion junctions at synapses and dendritic spines in area CA1 of the rat hippocampus. J. Comp. Neurol. 393, 58–68.

48. Lieberman, A.R., and Spacek, J. (1997). Filamentous contacts: the ultrastructure and three-dimensional organization of specialized non-synaptic interneuronal appositions in thalamic relay nuclei. Cell Tissue Res. 288, 43–57.

49. Perkins, G.A., Tjong, J., Brown, J.M., Poquiz, P.H., Scott, R.T., Kolson, D.R., Ellisman, M.H., and Spirou, G.A. (2010). The Micro-Architecture of Mitochondria at Active Zones: Electron Tomography Reveals Novel Anchoring Scaffolds and Cristae Structured for High-Rate Metabolism. J. Neurosci. 30, 1015–1026.

50. Shepherd, G.M., and Harris, K.M. (1998). Three-Dimensional Structure and Composition of CA3→CA1 Axons in Rat Hippocampal Slices: Implications for Presynaptic Connectivity and Compartmentalization. J. Neurosci. 18, 8300–8310.

51. Chang, D.T.W., Honick, A.S., and Reynolds, I.J. (2006). Mitochondrial trafficking to synapses in cultured primary cortical neurons. J. Neurosci. 26, 7035–7045.

52. Ryugo, D.K., Montey, K.L., Wright, A.L., Bennett, M.L., and Pongstaporn, T. (2006). Postnatal development of a large auditory nerve terminal: the endbulb of Held in cats. Hear. Res. 216–217, 100–115.

53. Kuenzel, T. (2019). Modulatory influences on time-coding neurons in the ventral cochlear nucleus. Hear. Res. 384, 107824.

54. Wickesberg, R.E., and Oertel, D. (1988). Tonotopic projection from the dorsal to the anteroventral cochlear nucleus of mice. J. Comp. Neurol. *268*, 389–399.

55. Justs, K.A., Lu, Z., Chouhan, A.K., Borycz, J.A., Lu, Z., Meinertzhagen, I.A., and Macleod, G.T. (2022). Presynaptic Mitochondrial Volume and Packing Density Scale with Presynaptic Power Demand. J. Neurosci. *42*, 954–967.

56. Takago, H., Oshima-Takago, T., and Moser, T. (2018). Disruption of Otoferlin Alters the Mode of Exocytosis at the Mouse Inner Hair Cell Ribbon Synapse. Front. Mol. Neurosci. *11*, 492.

57. Pulido, C., and Ryan, T.A. (2021). Synaptic vesicle pools are a major hidden resting metabolic burden of nerve terminals. Sci. Adv. *7*, eabi9027.

58. Perkins, G., Renken, C., Martone, M.E., Young, S.J., Ellisman, M., and Frey, T. (1997). Electron tomography of neuronal mitochondria: three-dimensional structure and organization of cristae and membrane contacts. J. Struct. Biol. *119*, 260–272.

59. Steyer, A.M., Ruhwedel, T., Nardis, C., Werner, H.B., Nave, K.-A., and Möbius, W. (2020). Pathology of myelinated axons in the PLP-deficient mouse model of spastic paraplegia type 2 revealed by volume imaging using focused ion beam-scanning electron microscopy. J. Struct. Biol. *210*, 107492.

60. Perkins, G.A., Song, J.Y., Tarsa, L., Deerinck, T.J., Ellisman, M.H., and Frey, T.G. (1998). Electron tomography of mitochondria from brown adipocytes reveals crista junctions. J. Bioenerg. Biomembr. *30*, 431–442.

61. Reisinger, E., Bresee, C., Neef, J., Nair, R., Reuter, K., Bulankina, A., Nouvian, R., Koch, M., Bückers, J., Kastrup, L., et al. (2011). Probing the functional equivalence of otoferlin and synaptotagmin 1 in exocytosis. J. Neurosci. *31*, 4886–4895.

62. Mastronarde, D.N. (2005). Automated electron microscope tomography using robust prediction of specimen movements. J. Struct. Biol. *152*, 36–51.

63. Butola, T., Wichmann, C., and Moser, T. (2017). Piccolo Promotes Vesicle Replenishment at a Fast Central Auditory Synapse. Front. Synaptic Neurosci. *9*, 14.

64. Mendoza Schulz, A., Jing, Z., Sánchez Caro, J.M., Wetzel, F., Dresbach, T., Strenzke, N., Wichmann, C., and Moser, T. (2014). Bassoon-disruption slows vesicle replenishment and induces homeostatic plasticity at a CNS synapse. EMBO J. *33*, 512–527.

65. Yang, H., and Xu-Friedman, M.A. (2008). Relative roles of different mechanisms of depression at the mouse endbulb of Held. J. Neurophysiol. *99*, 2510–2521.

66. Chakrabarti, R., Michanski, S., and Wichmann, C. (2018). Vesicle sub-pool organization at inner hair cell ribbon synapses. EMBO Rep. *19*, e44937.

67. Wong, F.K., Nath, A.R., Chen, R.H.C., Gardezi, S.R., Li, Q., and Stanley, E.F. (2014). Synaptic vesicle tethering and the CaV2.2 distal C-terminal. Front. Cell. Neurosci. *8*, 71.

68. Michanski, S., Smaluch, K., Steyer, A.M., Chakrabarti, R., Setz, C., Oestreicher, D., Fischer, C., Möbius, W., Moser, T., Vogl, C., and Wichmann, C. (2019). Mapping developmental maturation of inner hair cell ribbon synapses in the apical mouse cochlea. Proc. Natl. Acad. Sci. USA *116*, 6415–6424.

STAR★METHODS

KEY RESOURCES TABLE

REAGENT or RESOURCE	SOURCE	IDENTIFIER
Chemicals, peptides, and recombinant proteins		
Osmium tetroxide, 4% aqueous solution	EMS	Cat. No. 19170
Osmium tetroxide, christalline	EMS	Cat. No. 19132
UranyLess	EMS	Cat. No. 22409
Glutaraldehyde	Sigma-Aldrich	Cat. No. G7651
Potassium ferrocyanide, 2% aqueous solution	EMS	Cat. No. 25154-2
Critical commercial assays		
EPON Agar pre-mix kit	Plano	Cat. No: R1140
Durcupan ACM embedding mixture	Sigma-Aldrich	Cat. No: 44610
Epoxy Conductive Adhesive	EMS	EPO-TEK EE 129–4
Experimental models: Organisms/strains		
C57BL6/J mice	Jackson's Laboratory	Strain #:000664; RRID:IMSR_JAX:000664
Otof^{-/-} mice	Reisinger et al.,[61]	PMID: 21451027
Software and algorithms		
Excel	Microsoft (https://microsoft.com/mac/excel)	RRID:SCR_016137
Fiji software	Fiji (http://fiji.sc)	RRID: SCR_002285
GraphPad Prism software	GraphPad Prism (https://graphpad.com)	RRID:SCR_002798
Igor Pro software package	Wavemetrics (http://www.wavemetrics.com/products/igorpro/igorpro.htm)	RRID: SCR_000325
SerialEM	Mastronarde[62] (https://bio3d.colorado.edu/SerialEM/)	PMID: 16182563
3dmod	Kremer et al.[43] (https://bio3d.colorado.edu/imod/doc/3dmodguide.html)	PMID: 8742726
Amira	Thermo Fisher Scientific	Version 6.0.1

RESOURCE AVAILABILITY

Lead contact
Further information and requests for resources should be directed to and will be fulfilled by the Lead Contact, Carolin Wichmann (carolin.wichmann@med.uni-goettingen.de).

Materials availability
This study did not generate new unique reagents.

Data and code availability
All data reported in this paper will be shared by the lead contact upon request.

This paper does not report original code.

Any additional information required to reanalyze the data reported in this paper is available from the lead contact upon request.

EXPERIMENTAL MODEL AND SUBJECT DETAILS

Animals
C57BL/6J (wild-type, wt) and otoferlin knockout (*Otof*^{-/-}) mice[61] which were in a C57BL/6N background at postnatal (P) day 10, P21/22, and six-month-old animals (6M) of either sex were used for this study. Mice were housed in individually ventilated cages in groups with *ad libitum* access to food and water. All experiments were performed in compliance with the national animal care guidelines and were approved by the animal welfare of the University of Göttingen and the State of Lower Saxony.

METHOD DETAILS

Vibratome slice preparation

The samples were generated for the study Hintze et al. (2021)[31], and sample blocks as well as prepared grids from Hintze et al. (2021) [31], generated as described below, were reused for tomogram acquisition of presynaptic mitochondria. Notably, all tomograms used in this study were freshly acquired and not reused from Hintze et al. (2021).[31] 150 μm parasagittal slices of cochlear nuclei were prepared as described previously.[31,63–65] Mice were sacrificed with carbon dioxide and decapitated. Brains were dissected and immersed in ice-cold cutting solution containing (in mM) 50 NaCl, 26 NaHCO$_3$, 120 sucrose, 1.25 NaH$_2$PO$_4$xH$_2$O, 2.5 KCl, 20 glucose, 0.2 CaCl$_2$, 6 MgCl$_2$, 0.7 Na L-ascorbate, 2 Na pyruvate, 3 myo-inositol, and 3 Na L-lactate with an osmolarity of around 310 mOsm, pH adjusted to 7.35, continuously aerated with carbogen (95% O$_2$, 5% CO$_2$). The meninges were removed, and hemispheres were separated by a midsagittal cut. The forebrain was removed at the pons-midbrain junction and the remaining brain containing the brainstem and the cerebellum were glued onto the specimen plate of a VT 1200 S vibratome (Leica microsystems, Wetzlar, Germany) with the lateral sides facing upwards and the ventral side facing the blade. The specimen plate was then transferred to the buffer tray containing ice-cold cutting solution. Sections were cut at a blade feed rate of 0.02 mm/s with an amplitude of 1.50 mm. Slices containing the AVCN were trimmed and prepared for high-pressure freezing.

High-pressure-freezing

Slices of the AVCN were mounted onto type A specimen carriers (Leica Microsystems, Wetzlar, Germany) with a diameter of 3 mm and a depth of 0.2 mm, filled with cutting solution (see also above: (in mM) 50 NaCl, 26 NaHCO$_3$, 120 sucrose, 1.25 NaH$_2$PO$_4$xH$_2$O, 2.5 KCl, 20 glucose, 0.2 CaCl$_2$, 6 MgCl$_2$, 0.7 Na L-ascorbate, 2 Na pyruvate, 3 myo-inositol, and 3 Na L-lactate with an osmolarity of around 310 mOsm, pH adjusted to 7.35. The flat side of the type B carriers (Leica Microsystems, Wetzlar, Germany) was dipped in 1-hexadecene (Sigma-Aldrich, Wetzlar, Germany) and placed onto the type A carrier. Samples were frozen immediately using a HPM100 (Leica Microsystems, Wetzlar, Germany) and transferred into liquid nitrogen for storage or further processing.

Freeze-substitution

Freeze-substitution was performed in an EM AFS2 (Leica Microsystems, Wetzlar, Germany) as described previously.[66,67] The slices were incubated in 0.1% (w/v) tannic acid in acetone at −90°C for 4 days and then washed three times for 1 h each in acetone at −90°C. 2% (w/v) osmium tetroxide in acetone was applied and incubated for 40.4 h. The temperature maintained at −90°C for 7 h, before it rose to -20°C within another 14 h (5°C/h). Over a period of 14.5 h the temperature further rose to 4°C (10°C/h). At 4°C, osmium tetroxide was removed, the samples were washed three times with acetone and brought to room temperature. Slices were infiltrated in epoxy resin (Agar-100 kit, Plano, Germany; epoxy/acetone 1:1 3-6 h; 100% epoxy resin overnight), further incubated for additional 6 h in fresh 100% epoxy resin end placed in embedding molds.

Ultrathin-sectioning and post-staining

After polymerization for 48 h at 70°C, excess epoxy resin was removed with a fine file (DiATOME, Nidau, Switzerland) and the block was trimmed to a pyramid using a razor blade. To check the region and the structural preservation, 70 nm ultrathin sections were cut with a diamond knife (DiATOME, Nidau, Switzerland) using an EM UC7 (Leica Microsystems, Wetzlar, Germany) ultramicrotome. Sections were collected on formvar-coated copper slot grids (slot; Athene, Plano, Wetzlar, Germany). For electron tomography, 250 nm semi-thin sections were obtained and collected on formvar-covered mesh grids (100 mesh; Athene, Plano, Wetzlar, Germany). Poststaining was performed with UranyLess (EMS, Hatfield, PA) for 20 minutes at RT.

Electron tomography of presynaptic mitochondria

Samples (blocks) as well as grids already prepared for the analysis of endbulb of Held AZs, as mentioned above[31] were used and additionally, new grids were made. The region and the quality of the tissue were checked with 2D electron microscopy at 80 kV using a JEM1011 transmission electron microscope (JEOL, Freising, Germany) equipped with a Gatan Orius 1200A camera (Gatan, Munich, Germany). 10 nm gold beads (British Bio Cell/Plano, Germany) were applied to both sides of the stained grids with the 250 nm semithin-sections and electron tomography was performed as described previously.[66,67] For each animal, tomograms were acquired from two different AVCN vibratome slices and different grids of the slice. For each grid, tomograms were taken from several endbulbs of Held, but partially also several tomograms from one terminal. Endbulbs of Held were identified by the appearance of a large presynaptic terminal contacting the principal cell that show a clear SV cluster (Figure S1). For analysis, only terminals that additionally depicted AZs and a pronounced postsynaptic density (PSD), which was identifiable in the final tomogram, were considered. Synaptic terminals contacting dendrites within the AVCN with an asymmetric (denoted as PSD) synaptic site were chosen and classified as non-endbulb synapses. Tilt series from presynaptic mitochondria were acquired at 200 kV using a JEM2100 transmission electron microscope (JEOL, Freising, Germany) mostly from −60° to +60° with a 1° increment at 8-12,000× using the Serial-EM software package.[62] Tomograms were generated using the IMOD package etomo.[43]

Model rendering and image analysis

Tomograms were segmented manually using 3dmod,[43] with a pixel size of 1.648-1.188 nm. To measure mitochondrial volumes, their outer membranes were manually segmented on every 15th virtual section using the *sculpt* drawing tool and the contours were interpolated across

the Z-stack using the *interpolator* tool of 3dmod. Similarly, the crista membranes (CM) were manually segmented on every 5th virtual section. Mitochondrial volumes, the individual CM surface areas and CM inner volumes were measured using the *info* tool. The individual surface areas and inner volumes were summed up to determine the total area and inner volume of the cristae. The CM density was calculated by dividing the total CM surface area by the mitochondrial volume. The crista shape factor, which measures the lamellarity of CMs, was determined by dividing the total CM surface area and the total inner volume of the CMs.

Focused ion beam-scanning electron microscopy (FIB-SEM)

For FIB-SEM mice were anesthetized with carbon dioxide and sacrificed by decapitation. Brains were dissected and immersion fixed with 2% paraformaldehyde (PFA) and 2.5% glutaraldehyde in 0.1 M cacodylate buffer (pH7.2) for 48 h at 4°C and subsequently washed with cacodylate buffer and phosphate-buffered saline (PBS). 150 μm parasagittal slices of AVCN were prepared in PBS und slices were embedded as described in Michanski et al. (2019).[68] First, slices were incubated with 2% osmium tetroxide and 1.5% potassium ferrocyanide in 0.1 M cacodylate buffer for 1-2 h on ice. Next, samples were washed five times in distilled water and treated with a thiocarbohydrazide solution for 20 min at room temperature. After five washing steps in distilled water, 2% osmium tetroxide in 0.1 M cacodylate buffer was applied for 2 h and samples were washed again in distilled water. Subsequently, slices were placed overnight in 2.5% uranyl acetate in the dark. After washing in distilled water, samples were contrasted in Reynold's lead citrate for 30 min at 60°C, again washed in distilled water, dehydrated in increasing ethanol concentrations, and infiltrated in acetone with an increasing concentration of Durcupan (25%, 50%, 75% Durcupan in acetone for 1 h each and 100% Durcupan overnight). After polymerization for 48 h at 60°C, blocks were trimmed as described above for epoxy blocks and the region and quality of the tissue was assessed with a JEM1011 transmission electron microscope (JEOL, Freising, Germany) equipped with a Gatan Orius 1200A camera (Gatan, Munich, Germany).

For FIB-SEM, samples were trimmed with a 90° diamond trimming knife (DiATOME, Nidau, Switzerland) and the trimmed part was cut from the Durcupan block and glued onto a SEM stub (Science Services GmbH, Munich, Germany, Pin 12.7 mm x 3.1 mm) by a silver filled epoxy (Epoxy Conductive Adhesive, EPOTEK EE 129-4; EMS, Hatfield, PA) and polymerized at 70°C overnight. Samples were coated with a 10 nm gold layer using the sputter coating machine EM ACE600 (Leica Microsystems, Wetzlar, Germany) at 30 mA current, placed into the Crossbeam 540 FIB-SEM (Carl Zeiss Microscopy GmbH, Jena, Germany) and positioned at an angle of 54°. To protect the surface of the tissue and ensure even milling, a 400 nm platinum layer was deposited on top of the region of interest. Atlas 3D (Atlas 5.1, Fibics, Canada) software was used to collect the 3D data. To open up trenches to expose a cross-section through the sample a 15/30 nA current was used, while a 7 nA current was used to polish the cross-section surface. The images were acquired at 1.5 kV with the ESB detector (450 V ESB grid, pixel size x/y 2 or 5 nm) in a continuous mill and acquire mode using 700 pA or 1.5 nA for the milling aperture (z-step 5 or 8 nm). For post processing, data were aligned using the plugin "Linear Stack Alignment with SIFT" or "TrakEM", inverted and cropped in Fiji. Depending on the properties of the data set, a Gaussian blur of 0.5 to 2, a local contrast enhancement using a CLAHE plugin in Fiji, a smoothing function, and a binning by 2 or 3 in x/y was applied.

The FIB-SEM imaging data was analyzed in IMOD. The mitochondrial occupation of presynapses was determined by manual counting of presynapses that were visible in the field of view. Thereby, we discarded presynapses that were only partially imaged e.g., close to the image borders. Next, the fraction of presynapses containing mitochondria was determined by manual inspection.

3D models of presynaptic boutons were created using IMOD segmentation tools. For each material, a combination of manual segmentation and smooth interpolation was used. Finally, the volume of the segmented boutons, the PSDs and mitochondria were determined using Amira 6.0.3. Final volumes of the material in μm³ were obtained by the voxel count extracted in Amira multiplied by the individual voxel sizes of the image datasets. Synaptic vesicles were segmented as scattered materials and the total number for each bouton was directly determined in IMOD.

QUANTIFICATION AND STATISTICAL ANALYSIS

Data were analyzed using *Excel*, *Igor Pro 8.1* (Wavemetrics), and *GraphPad Prism 9.4.1* (GraphPad Software). Normal distribution was assessed with the Jarque-Bera test and equality of variances was assessed with the *F*-test in normally distributed data. For two-sample tests and normally distributed data, two-tailed unpaired t-test (T), or, when not normally distributed, the Wilcoxon rank test (W) was used. *For more than two datasets*, one way ANOVA with post-hoc correction by Tukey's test was used to detect differences for normally distributed data. For not normally distributed data, Kruskal-Wallis (KW) test followed by Dunn's test was used.